THE JOURNAL OF PHYSICAL CHEMISTRY A
A JOURNAL OF THE AMERICAN CHEMICAL SOCIETY

pubs.acs.org/JPCA Article

Electric Field-Induced Water Condensation Visualized by Vapor-Phase Transmission Electron Microscopy

Yuhang Wang, Dewansh Rastogi, Kotiba Malek, Jiayue Sun, Akua Asa-Awuku,* and Taylor J. Woehl*

Cite This: *J. Phys. Chem. A* 2023, 127, 2545−2553 Read Online

ACCESS | Metrics & More | Article Recommendations | Supporting Information

ABSTRACT: Understanding the nanoscale water condensation dynamics in strong electric fields is important for improving the atmospheric modeling of cloud dynamics and emerging technologies utilizing electric fields for direct air moisture capture. Here, we use vapor-phase transmission electron microscopy (VPTEM) to directly image nanoscale condensation dynamics of sessile water droplets in electric fields. VPTEM imaging of saturated water vapor stimulated condensation of sessile water nanodroplets that grew to a size of ∼500 nm before evaporating over a time scale of a minute. Simulations showed that electron beam charging of the silicon nitride microfluidic channel windows generated electric fields of $\sim 10^8$ V/m, which depressed the water vapor pressure and effected rapid nucleation of nanosized liquid water droplets. A mass balance model showed that droplet growth was consistent with electric field-induced condensation, while droplet evaporation was consistent with radiolysis-induced evaporation *via* conversion of water to hydrogen gas. The model quantified several electron beam−sample interactions and vapor transport properties, showed that electron beam heating was insignificant, and demonstrated that literature values significantly underestimated radiolytic hydrogen production and overestimated water vapor diffusivity. This work demonstrates a method for investigating water condensation in strong electric fields and under supersaturated conditions, which is relevant to vapor−liquid equilibrium in the troposphere. While this work identifies several electron beam−sample interactions that impact condensation dynamics, quantification of these phenomena here is expected to enable delineating these artifacts from the physics of interest and accounting for them when imaging more complex vapor−liquid equilibrium phenomena with VPTEM.

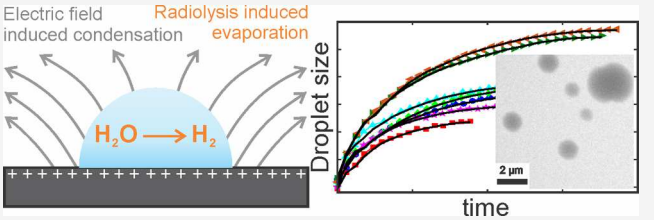

INTRODUCTION

Water condensation in electric fields is important to understand vapor−liquid equilibrium in clouds and thunderstorms.[1−3] Aside from relevance to atmospheric sciences, electric field-induced condensation is also seeing increasing interest as a method to directly capture atmospheric moisture.[4,5] Prior works have demonstrated that electric fields can cause water vapor condensation under saturated or subsaturated conditions and that electric fields accelerate water droplet growth.[1,2,6,7] Theoretical calculations have shown that electric fields of $>10^7$ V/m induce water condensation by decreasing the water vapor pressure.[3,8] However, prior work has mainly focused on the effect of electric fields on micron-sized or larger water droplets.[9] Aside from scanning probe microscopy studies with highly localized electric fields,[6] no work has established how electric fields impact nucleation and growth of nanosized sessile water droplets.

Prior work has utilized atomic force microscopy (AFM) and environmental transmission electron microscopy (ETEM) to visualize sessile droplet formation, but AFM is limited to local application of electric potentials, while ETEM is limited to low total pressures (∼10 mbar) that are not relevant to atmospheric processes.[10−12] On the other hand, in situ gas-phase and liquid-phase TEM using microfabricated, hermetically sealed microfluidic chambers are capable of visualizing liquid and solid particles with sizes as small as a few nanometers under atmospherically relevant conditions.[13] In these experiments, the liquid or gas can be held at atmospheric pressure and the temperature controlled between room temperature and the normal boiling point of water. For instance, prior work has utilized liquid-phase TEM to investigate nanoscale droplet transport dynamics on a flat solid surface,[14] wetting of water films on nanostructured surfaces,[15] and the behavior of nanoscale bubbles in water.[16−19] TEM beam electrons have energies ranging from 100 to 300 keV, which ionize in the sample and cause omnipresent electron beam effects such as heating, electric charging, and radiolysis.[17,20−23] While these electron beam−sample interactions have been thoroughly explored for liquid-phase nanoparticle synthesis and organic samples,[24,25] their impact on aerosol-phase phenomena remains unknown. Cataloging and quantifying how the electron beam impacts

Received: November 22, 2022
Revised: February 10, 2023
Published: March 13, 2023

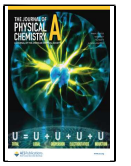

https://doi.org/10.1021/acs.jpca.2c08187
J. Phys. Chem. A 2023, 127, 2545−2553

aerosol-phase phenomena (condensation, evaporation, and nucleation) and the associated physical parameters (humidity, diffusivity, and temperature) during in situ TEM is critical to delineating these phenomena from the aerosol phenomena of interest. In this article, we directly image the nucleation, growth, and evaporation of nanoscale sessile drops with vapor-phase TEM (VPTEM). We developed quantitative and self-consistent models for the electron beam-induced electric field, droplet nucleation energetics, droplet growth kinetics, and water radiolysis. Together, the models show that droplet nucleation and growth were stimulated by vapor pressure depression by electron beam-induced electric fields (~10^8 V/m), while droplet evaporation was consistent with radiolytic conversion of water to hydrogen gas (Figure 1a). This work

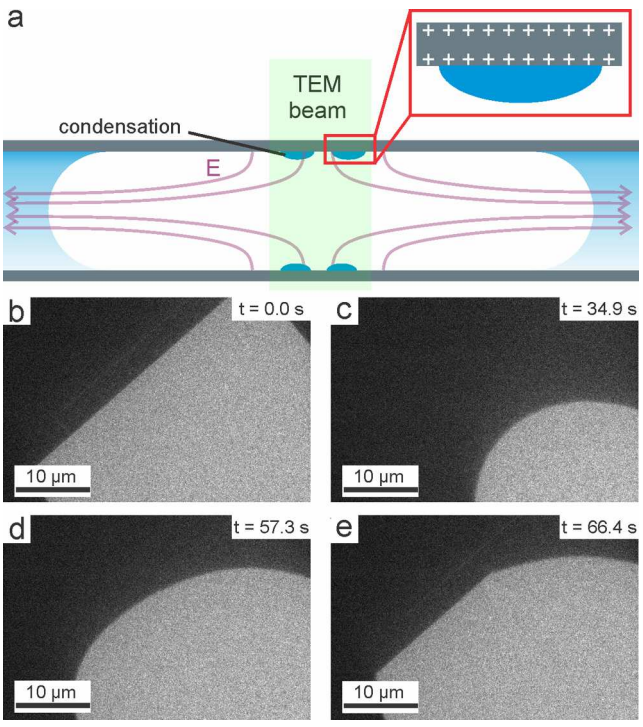

Figure 1. Schematic cartoon of the experimental setup and vapor bubble formation during VPTEM. (a) Schematic of the VPTEM experiment (not to scale). The silicon nitrides membranes are shown in gray, the bubble is shown in white, surrounding water in blue, and condensing water droplets as blue hemispheres on the silicon nitride windows. The purple lines represent the divergent electric fields emanating from the positively charged silicon nitride. The inset red box shows a zoomed-in region of the top silicon nitride membranes showing the accumulation of charge at each surface, which creates a large divergent electric field. (b–e) Time-lapsed VPTEM images showing the initially dry microfluidic sample cell (b) and the process of vapor bubble formation over the silicon nitride windows (c–e).

provides the first quantitative measurements of electron beam–sample interactions for a model aerosol-phase process. The results contribute foundational knowledge required to apply VPTEM to investigate more complex aerosol phenomena, including cloud condensation nucleation, condensation and moisture capture in electric fields, ice nucleation, secondary aerosol formation, and aerosol aging.

EXPERIMENTAL METHODS

Sample Preparation and VPTEM. A liquid-phase TEM holder (Protochips Poseiden Plus, USA) was used in the VPTEM experiments. The sample cell consisted of two sample chips, each of which consisted of an electron transparent freestanding 50 nm silicon nitride membrane supported by a silicon substrate. Both chips were washed with acetone and methanol and underwent plasma treatment with air plasma (Harrick Plasma, PDC-32G) for 45 s before assembling to eliminate carbon contamination. The sample was assembled several hours after plasma cleaning to diminish the hydrophilic effects of the plasma because hydrophobic sample surfaces enable formation of a large vapor bubble. The sample was assembled by sandwiching two chips together, separated by 150 nm thick gold spacers on one chip, with air in between. Prior work has shown that actual separation between the two silicon nitride membranes is 500–1000 nm due to membrane bulging and particulate contamination.[26] The microfluidic lines of the sample holder were dried prior to the experiments by filling with ethanol and then vacuum pumping overnight to evaporate all liquid. All TEM experiments were performed on a JEOL JEM-2100F operating in the TEM mode at 200 kV accelerating voltage. The electron beam current was measured by impinging the TEM beam onto a charge-coupled device detector (Gatan Image Filter) with the current output from the detector attached to an electrometer, which showed that the electron beam current was i_e = 6.54 nA. TEM videos were recorded at a frame rate of 10 fps by the Camtasia Studios screen capture software and processed in ImageJ and VideoMach. Custom scripts written in Matlab were used to track the growth of droplets in the VPTEM movies.

Electric Field Simulations. The electrostatics module in COMSOL 5.6 was used to compute the electric field in the sample cell prior to droplet condensation. The model solved Gauss's law, $\nabla \boldsymbol{E} = \frac{\rho_f}{\epsilon\epsilon_0}$, in 2D over the cross section of the microfluidic device, where ρ_f is the surface free charge density, $\boldsymbol{E}$ is the electric field vector, ϵ is the relative permittivity of the corresponding material, and ϵ_0 is the vacuum permittivity. The simulation geometry is shown in the Supporting Information and is approximately the dimensions of a 2D cross section through the sample cell (Figure S1). Preset values for dielectric constants and conductivities were utilized except for the silicon nitride conductivity, which was 1×10^{-13} S/m, and relative permittivity, which was $\epsilon = 7$.

Radiolysis Simulations. We utilized the model of Schneider et al. to estimate the hydrogen production rate in the water droplets as a function of time.[21] This model solves a set of 16 coupled time-dependent ordinary differential equations (ODEs) for the reaction kinetics of 16 primary and secondary radiolysis species

$$\frac{\partial c_i}{\partial t} = -\sum_j k_{ij} c_i c_j + \sum_{j,k\neq i} k_{jk} c_j c_k + \mathfrak{R}_i \tag{1}$$

Here, c_i is the radiolysis product concentration, k_{ij} denotes the known reaction rate constants, and $\mathfrak{R}_i$ represents the volumetric production rate of species i due to radiolysis by the electron beam.

$$\mathfrak{R}_i = \frac{\rho_W \psi G_i}{F} \tag{2}$$

Here, G_i refers to the G-values for each radiolysis species, empirical parameters for the production rate of each primary radiolysis species in units of molecules/100 eV absorbed, ρ_W is the density of water, ψ is the stopping power, and F is

https://doi.org/10.1021/acs.jpca.2c08187
J. Phys. Chem. A 2023, 127, 2545–2553

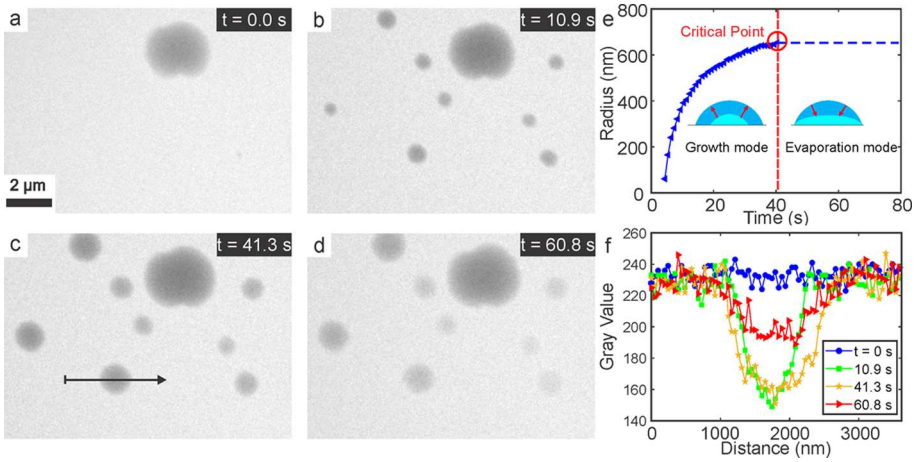

Figure 2. Electron beam-induced water droplet condensation. (a–d) Time lapsed VPTEM images showing sessile droplet nucleation, growth, and evaporation. (e) Change in the droplet radius as a function of time measured from the projected area. The red circle and dashed vertical line denote the critical radius and time where the droplet stopped growing. The dashed horizontal line after the critical point indicates that the projected droplet radius remained the same during droplet evaporation. (f) Intensity profiles of the droplet marked by the black arrow in (c) for different times.

Faraday's constant. We utilized literature values for each parameter above from Wang et al. or Pastina and LaVerne (see *G*-values in Table S1).[26,27] The coupled set of ODEs were solved numerically using a Runge–Kutta method in Mathematica for the concentration of each species as a function of time, assuming homogeneous reactions within the droplets.[21] Additional details of the simulations are given in the Supporting Information.

RESULTS AND DISCUSSION

VPTEM imaging was carried out in a closed microfluidic sample cell created by sandwiching a thin (<1 μm) layer of water or vapor between two freestanding 50 nm thick silicon nitride films (see Experimental Methods, Figure 1a). Bubbles with approximate dimensions on the order of 50 × 500 × 1 μm, the dimensions of the space between the freestanding silicon nitride windows, were generated inside the microfluidic cell during TEM (Figure 1a). The microfluidic cell and fluid lines were initially filled with room-temperature air and imaged at a low magnification while deionized water was injected (Figure 1b; see Supporting Information, Movie S1, for full data set). The water partially filled the viewing area, indicated by the appearance of new dark contrast regions within the window area in Figure 1c. However, due to a combination of radiolytic generation of hydrogen gas and the hydrophobic silicon nitride surface,[20] water did not completely fill the sample cell and instead a bubble formed and grew over the electron transparent region of silicon nitride (bottom right, Figure 1d,e). The bubble size and shape remained stable indefinitely after the fluid flow ceased.

The bubble was entirely surrounded by room-temperature liquid water, indicating that the water in the system was in vapor–liquid equilibrium. At equilibrium, the partial pressure of water (p_w) in the bubble was equal to the water vapor pressure, $p_W = p^*_{v,0}(23^\circ\mathrm{C}) = 3.17$ kPa, and the supersaturation ratio of water in the vapor phase was $S = \frac{p_W}{p^*_{v,0}} = 1$. Under these conditions, there was no thermodynamic driving force for water condensation within the gas bubble. Imaging the gas bubble with a >28 μm TEM beam radius and a beam current of i_e = 6.54 nA resulted in no water condensation. However, condensing the TEM beam to a smaller radius caused rapid nucleation and growth of sessile water drops in the bubble on the silicon nitride surface. Figure 2a shows a frame from a TEM movie taken within the gas bubble, where the large water droplet in the top right was from a prior experimental trial and was not included in subsequent analysis and modeling (see the uncropped TEM data in Supporting Information Movie S2 and Supporting Information Movie S3 for an experimental replicate). Condensing the electron beam to 24 μm in radius caused rapid nucleation of water droplets on the silicon nitride surface within seconds (Figure 2b). Nanosized sessile water droplets appeared on the surface and grew with a non-constant rate until a time of ~40 s (Figure 2c,d). The droplet radius increased more rapidly immediately after nucleation, and the rate slowed over time until a critical point after which growth halted (Figure 2e). After the critical point, the sessile droplets retained their projected area but were observed to decrease in image contrast over time (Figure 2f). Based on the mass-thickness contrast mechanism of TEM, the decrease in image contrast within the droplets indicated that the water thickness decreased due to evaporation. At higher magnification and smaller TEM beam diameter of ~500 nm that produced larger electron fluxes, thick columns of water formed that spanned between the two silicon nitride membranes (Figure S2).

Inelastic electron scattering of the TEM electron beam in the sample causes radiolysis of water molecules,[25] sample heating,[17] and electrical charging of the silicon nitride membranes.[20,28] The former two are not expected to condense water because they will not modify the supersaturation ratio of water vapor. In fact, radiolysis is expected to convert water molecules to hydrogen gas, effectively causing evaporation. Electron beam charging occurs due to secondary electron (SE) and Auger electron (AE) emission from the insulating silicon nitride windows into the vacuum, which leaves behind positively charged holes that cannot be fully neutralized by current from the ground.[28] The result is a divergent electric field oriented normal to the silicon nitride surface and directed away from the image area (*cf.* Figure 1a).[29] Below, we develop scaling models using conventional electrostatics and nucleation

https://doi.org/10.1021/acs.jpca.2c08187
J. Phys. Chem. A 2023, 127, 2545–2553

and transport theories to estimate the electric field during VPTEM and its effect on water condensation dynamics.

Charge accumulation in irradiated silicon nitride can be determined by balancing the AE and SE emission currents with neutralizing current from the ground.[28] In insulating films, the current from the ground does not completely balance the AE and SE emission current, so a positive charge accumulates in the film. Based on the analytical thin film model by Cazaux, the total charge (Q) in the irradiated region at steady state is related to the TEM beam current, SE and AE electron yield, and the electrical conductivity of the film by[28]

$$Q = \frac{i_e(\delta^x + y^x)\epsilon\epsilon_0}{\sigma} \tag{3}$$

Here, i_e = 6.45 nA is the measured beam current, δ^x is the SE yield, y^x is the AE yield, $\epsilon\epsilon_0 = 7 \times 8.85 \times 10^{-12}$ F/m is the dielectric permittivity of silicon nitride, and σ is the electrical conductivity of silicon nitride. Based on prior literature, we approximate the total SE and AE yield to be $\delta^x + y^x \approx 10^{-4}$.[28] Due to a lack of consistent literature values for the electrical conductivity of the low stress amorphous silicon nitride used in these experiments, which can vary between 10^{-12} and 10^{-14} S/m, we used this as a fitting parameter. A value of $\sigma = 1 \times 10^{-13}$ S/m yielded an electric field magnitude equivalent to the value derived by fitting a mass and energy balance model to the experimental water droplet growth kinetics as shown later in this article.

Due to the relatively low mobility edge of amorphous insulators, the free positive charges generated in silicon nitride are expected to be mobile and migrate to the surfaces of the membranes by diffusion and electromigration. Once at the surface, it is possible that the free positive charges spread to minimize repulsive Coulombic forces or become neutralized by SEs; however, this complexity cannot be readily included using the scaling analysis approaches used here. For simplicity, we assume that the free positive charges remain within the electron-irradiated region and coat each side of the silicon nitride membranes equally. The surface free charge density on each side of the silicon nitride membranes can then be estimated by dividing the total accumulated charge determined by eq 3 by twice the surface area of the electron beam-irradiated area

$$\rho_f = \frac{Q}{2A_{surf}} \tag{4}$$

where ρ_f is the surface free charge density, $A_{surf} = \pi r_{beam}^2$ is the surface area of the irradiated silicon nitride film, r_{beam} = 24 μm is the electron beam radius at the time of droplet nucleation, and the factor of 2 in the denominator accounts for division of the free charge between both surfaces of the film (Figure S1a). The electric field resulting from this positive charge accumulation on the silicon nitride membranes was simulated by numerically solving Gauss's law in two dimensions using finite element analysis. In brief, the electron beam-illuminated regions of silicon nitride were modeled with constant surface free charge density of ρ_f on each side, while the rest of the film and surrounding air and vacuum had zero free charge density (Figure S1b). We assumed that the electron flux and the TEM beam radius were the same on both silicon nitride membranes. Given the small convergence angle of the TEM beam at low image magnifications used here (<5 mrad) and the ~1 μm gap between the membranes, the change in the beam size from the top to the bottom windows will be small compared to the beam size. Likewise, nearly 100% of the incident electron beam transmits through the top silicon nitride window and water vapor, indicating that electron flux should not decrease significantly at the bottom window compared to the top window. The resulting large positive potentials in each silicon nitride membrane generated divergent electric fields normal to the surfaces of the silicon nitride membrane surfaces (Figure 3a). Figure 3b shows the y-component of the electric field

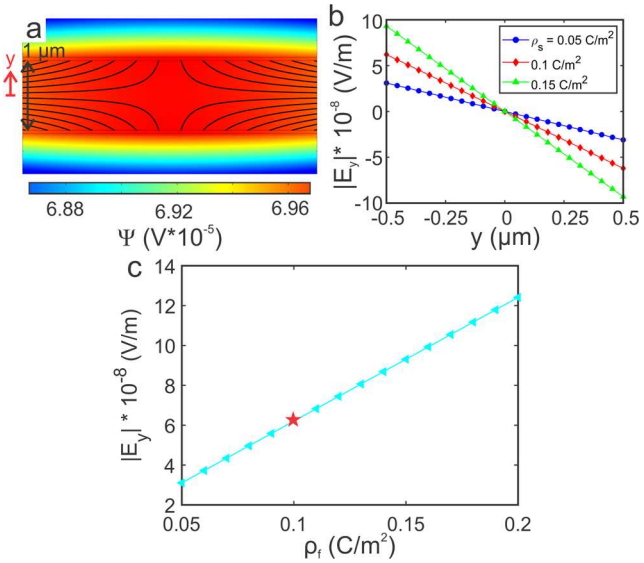

Figure 3. Electrostatic model for electron beam charging-induced electric fields. (a) Modeled electric field and electric potential spatial distribution for a surface free charge density of 0.1 C/m^2 on each side of the silicon nitride membranes. Electric field lines diverge away from both membranes into the air gap and away from the electron beam-irradiated region. (b) Magnitude of the electric field in the y-direction between the two silicon nitride membranes for several surface free charge density values. (c) Maximum electric field magnitude normal to the top silicon nitride membrane as a function of surface free charge density. The red star shows the electric field magnitude and surface free charge density corresponding to the image conditions used in Figure 2.

between the two silicon nitride membranes, which was negative and maximum at the inner surface of the top window, decreased to zero in the cell center, and then became positive as it approached the bottom membrane. The magnitude of the electric field evaluated at the silicon nitride film surface where sessile water droplets nucleated was taken as the relevant electric field in the subsequent nucleation calculations (Figure 3c). The resulting electric field at the surface free charge density corresponding to the experimental electron flux was $|E| \approx 6 \times 10^8$ V/m, as shown by a red star. We note that this electric field is orders of magnitude larger than the breakdown strength of air, ~1×10^6 V/m. However, the breakdown strength of water vapor increases rapidly above 1×10^7 V/m at atmospheric pressure and room temperature for gap sizes below 100 μm.[30] Likewise, there are no electrically conductive paths between the electron-irradiated regions and electrical ground, so no current can flow in the system. While the electron scattering, free charge density in silicon nitride and electric field problems are fully coupled in the experimental system, this model approximates the system as decoupled by independently determining the surface free charge density to

https://doi.org/10.1021/acs.jpca.2c08187
J. Phys. Chem. A 2023, 127, 2545−2553

simplify the mathematical problem. Likewise, the scaling model assumes that all SEs and AEs generated in the films escape into the vacuum and does not consider neutralization of free positive surface charges by SEs and AEs. Despite decoupling the physics, this approach yields values that are consistent with the models for droplet growth and electric field-induced vapor pressure depression.

We propose that the large electric field magnitude normal to silicon nitride decreased the vapor pressure of water and created a supersaturated vapor phase where $p_W > p^*_{v,0}$ and $S > 1$, which effected water condensation *via* a nucleation and growth mechanism. According to a prior model by Butt et al., an electric field normal to a vapor−liquid interface effectively reduces the water vapor pressure, yielding a modified Kelvin equation[8]

$$\ln\left(\frac{p^*_{v,E}}{p^*_{v,0}}\right) = -\frac{V_m}{R_g T}\left[\frac{(\epsilon - 1)\epsilon_0}{2}|E|^2 - \frac{\sigma_a}{a}\right] \quad (5)$$

where $p^*_{v,E}$ is the vapor pressure of water accounting for surface curvature and electric field effects, V_m is the molar volume of liquid water, R_g is the universal gas constant, T is the temperature, $|E|$ is the electric field magnitude in water vapor, σ_a is the surface tension of water, and a is the droplet radius. Because the critical nucleus for liquid water is single nanometers in size, we must consider the size-dependent surface tension of water described by the Tolman equation, $\sigma_a = \frac{\sigma_0}{1+\frac{\delta}{a}}$, where $\sigma_0 = 72$ mJ/m^2 is the surface tension of bulk water and $\delta = 0.21$ nm is the Tolman length of water.[31] Equation 5 shows that increasing the electric field strength depresses the vapor pressure, while decreasing the droplet size increases the vapor pressure (Figure 4a). Vapor pressure depression is insignificant for electric field magnitudes of $<10^7$ V/m, while curvature effects become insignificant for droplet sizes of >100 nm. The electric field calculated by the electrostatics model, $\sim 6 \times 10^8$ V/m, decreased the vapor pressure of the droplet by about a factor of 2 to yield a supersaturation ratio of $S \approx 2$.

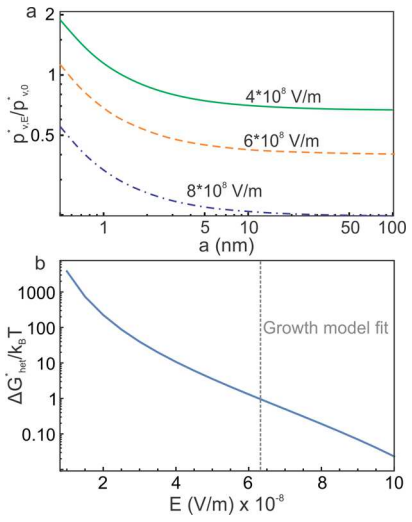

Figure 4. Model for electric field-induced water droplet nucleation. (a) Vapor pressure of water in an electric field normalized to vapor pressure above a flat surface as a function of water drop radius and electric field magnitude. (b) Critical free energy for heterogeneous nucleation as a function of electric field magnitude. The vertical dashed gray line denotes the electric field magnitude calculated for the experiments shown in Figure 2.

Liquid water is the thermodynamically stable phase under supersaturated vapor conditions, but there is a kinetic barrier to nucleation due to the positive Gibb's free energy associated with creating a new vapor−liquid interface. Classical nucleation theory shows that the critical free energy for nucleation is[32]

$$\Delta G^* = \frac{16\pi\sigma_a^3\nu^2}{3(k_B T)^2(\ln S)^2} \quad (6)$$

Here, k_B is Boltzmann's constant, $\nu = 2.99 \times 10^{-29}$ m^3 is the volume of a liquid water molecule, and ΔG^* is the critical free energy for nucleation. The impact of droplet wetting on the solid surface is considered in the model with the wetting parameter, $f(\theta)$, to determine the critical free energy for heterogeneous nucleation, $\Delta G^*_{het} = f(\theta)\Delta G^*$. The wetting parameter has the following functionality for a sessile droplet with a contact angle of θ

$$f(\theta) = \left[\frac{(2 + \cos\theta)(1 - \cos\theta)^2}{4}\right] \quad (7)$$

Prior measurements showed that the value of the macroscopic contact angle of a sessile water droplet on a silicon nitride membrane was $\theta = 51°$, which is used here.[20] Nucleation of water droplets is expected to occur rapidly with no lag time when the critical free energy for nucleation reaches $\Delta G^*_{het} \leq 1 k_B T$. Here, liquid water nucleates on the solid surface due to random fluctuations in the water vapor partial pressure, which eventually establishes clusters of water molecules larger than the critical nuclei size. Our model demonstrates that the critical nucleation energy reaches the thermal energy when the electric field reaches a magnitude of $\approx 6 \times 10^8$ V/m (Figure 4b), indicating that rapid nucleation is expected under the experimental conditions. Likewise, the critical free energy for nucleation increases rapidly above $1 k_B T$ for smaller values of the electric field, consistent with no nucleation when the electron flux was decreased.

We developed a transport model for the droplet growth kinetics to further test the proposed mechanism (see Supporting Information, Sections 3 and 4, for the detailed derivation). There are a couple of potential transport mechanisms that could transport water vapor to the surface of the growing droplet, including dipolar forces and diffusion. Dipolar forces act on permanent dipoles in an electric field gradient and create a dipolar force directed toward the highest electric field strength, $F_{dipole} = p\nabla|E|_y$, where p is the dipole moment of the molecule. Calculations based on the prior work of Gabyshev et al. show that the dipolar force on a single water vapor molecule in the field gradient calculated here is on the order $F_{dipole} \sim 10^{-15}$ N.[2] This force is 4 orders of magnitude smaller than the kinetic energy of a water molecule, $F_{KE} = \frac{\frac{3}{2}k_B T}{a_{H_2O}} = 10^{-11}$ N, where $a_{H_2O} = 0.2$ nm is the approximate effective radius of a water molecule. These calculations demonstrate that dipolar forces are negligible and diffusion is expected to be the main driving force transporting water molecules to the droplet surface. The droplet growth kinetics were therefore modeled with a mass balance that equated the rate of change of droplet mass with the product of the droplet

https://doi.org/10.1021/acs.jpca.2c08187
J. Phys. Chem. A 2023, 127, 2545−2553

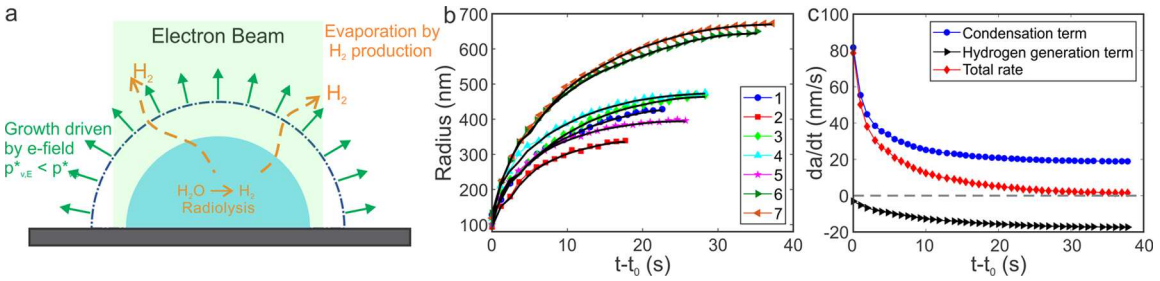

Figure 5. Mass and energy balance model for droplet growth kinetics. (a) Schematic of the electron beam effects on water condensation (not to scale). The electric field generated by the electron beam drove droplet growth by reducing the water vapor pressure (green arrows), while radiolysis converted liquid water to hydrogen gas, decreasing the growth rate and eventually causing evaporation (orange arrows). (b) Experimental growth curves for each droplet in Figure 2 with model fits to eq 9 shown as black lines. The nucleation time (t_0) was subtracted from each curve. (c) Rate of change in droplet radius for droplet 7 as a function of time (red diamonds) broken into the positive growth rate due to electric field-induced condensation (blue circles) and the negative growth rate due to radiolytic conversion of water to hydrogen (black triangles).

surface area and the diffusive flux of water vapor to the droplet surface. The sign of the flux is determined by whether the partial pressure of water is smaller (positive flux yields evaporation) or larger (negative flux yields condensation) than the vapor pressure of bulk water at the system temperature. Depletion of water vapor within the boundary layer near the droplet surface establishes a partial pressure gradient, which drives water vapor to condense on the droplet surface. The model included curvature effects on the water vapor pressure near the droplet surface, electric field-induced vapor pressure decrease, and radiolysis (Figure 5a). Radiolysis of water by high-energy electrons produces various radicals and molecules, $H_2O \rightarrow e_h^-, \dot{H}, \dot{O}H, H_2, H_2O_2, H_3O^+, \dot{H}O_2$.[20,24] Prior work has shown that irradiation of liquid water with a TEM beam can form significant amounts of hydrogen gas.[17] Radiolytic conversion of water to hydrogen gas was included in the droplet mass balance *via* a generic mass conversion rate of liquid water to hydrogen gas

$$\dot{m}_W = -R_{H_2} M_W V(t) \tag{8}$$

Here, R_{H_2} is the molar production rate of hydrogen gas, M_W is the molar mass of water, and $V(t)$ is the time-dependent volume of the droplet. There are several routes for water to be converted to hydrogen gas during radiolysis, each with a different reaction stoichiometry. The main conversion pathway from water to hydrogen involves a 1:1 molar conversion of water to hydrogen, so we assume that each mole of hydrogen produced consumes 1 mol of water. The mass conversion also assumes that all hydrogen gas produced leaves the water phase due to the low solubility of hydrogen in water (0.8 mM at room temperature). Finally, the change in temperature of the droplet is computed based on an energy balance that includes the latent heat of condensation and evaporation of water and electron beam-induced heating based on a previous model by Grogan et al.[17] For brevity, we show only the final analytical expression for the time derivative of droplet radius

$$\frac{da}{dt} \approx \frac{2M_W D_v^*(T_{drop}) \mathrm{Sin}^3\theta}{R_g \rho_W (2 + \mathrm{Cos}\theta)(1 - \mathrm{Cos}\theta) a} \left[\frac{p_{v,0}^*(T_\infty)}{T_\infty} - \frac{p_{v,E^*}(T_{drop})}{T_{drop}} \right] - \frac{R_{H_2} M_W a}{3 \times \rho_W} \tag{9}$$

Here, t is time, ρ_w is the density of liquid water, T_{drop} is the droplet temperature, T_∞ is the system temperature far from the droplet, $D_v^*(T_{drop})$ is the diffusion coefficient of water at the droplet temperature, $p_{v,0}^*(T_\infty)$ is the vapor pressure of water far from the droplet surface, and $p_{v,E}^*(T_{drop})$ is the vapor pressure of water at the droplet surface. Equation 9 shows that the change in the droplet radius is controlled by two processes: electric field-induced water condensation due to vapor pressure depression (first term on the right hand side) and radiolysis-induced evaporation due to conversion of liquid water to hydrogen gas (second negative term on the right hand side). Each phenomenon is active during the entire condensation/evaporation process but has a different dependency on the droplet radius and time.

We devised a protocol to fit the mass and energy balance expressions to the experimental droplet growth kinetics (see Supporting Information, Section 5, for details). In brief, each droplet growth trajectory showed a unique critical point where the growth rate decreased to zero, $\frac{da}{dt}(a_{crit}) = 0$, providing an algebraic equation for each of the seven droplets shown in Figure 2. There were three constant, unknown variables or variable groups in each algebraic equation that were considered as fitting parameters: the electric field magnitude, $|E|$, the molar rate of hydrogen gas production, R_{H_2}, and the product of water vapor diffusion coefficient and a geometric expression for droplet shape, $\varphi = \frac{D_v^*(T_{drop})\mathrm{Sin}^3\theta}{(2 + \mathrm{Cos}\theta)(1 - \mathrm{Cos}\theta)} = D_v^*(T_{drop}) g(\theta)$. The initial guesses for these parameters were obtained by fitting the linearized form of eq 9 to the experimental da/dt vs a data (Figure S6). Each of the seven critical point equations with initial guesses included for the fitting parameters were subtracted in pairs to generate seven residual values, and their sum was minimized by modifying the fitting parameters using a standard solver. The resulting values of the fitting parameters were then used to fit the droplet radius vs time data using droplet temperature (T_{drop}) as an additional fitting parameter. The sum of squared residuals was minimized for each droplet using standard approaches, resulting in the black fit lines in Figure 5b. The calculated droplet temperatures are provided in the Supporting Information and can be observed to fluctuate randomly with time and by ±10 K between adjacent droplets (Figure S7). The model showed excellent agreement with the experimental data with the temperature fluctuations in time likely due to noise in the growth rate data. Figure 5c illustrates the origin of the critical radius and critical time at which the droplets began to evaporate. The rate of

https://doi.org/10.1021/acs.jpca.2c08187
J. Phys. Chem. A 2023, 127, 2545−2553

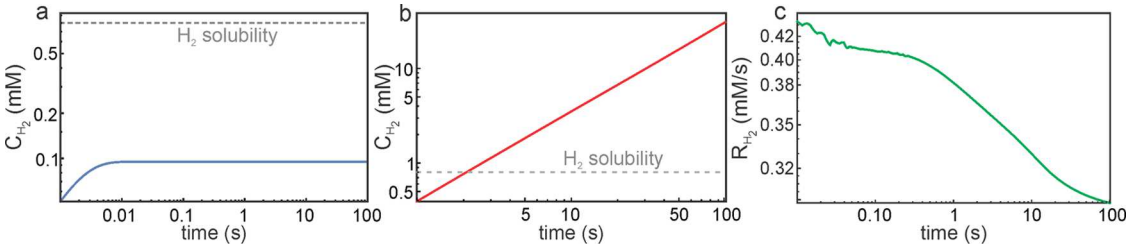

Figure 6. Radiolysis kinetic models for hydrogen production in water for 200 keV electrons and SBEs. (a) Hydrogen gas concentration as a function of time for 200 keV electrons with a dose rate of 1 MGy/s. The hydrogen solubility limit of 0.8 mM in water is shown by the dashed gray line. (b) Hydrogen gas concentration and (c) production rate as a function of time for SBEs with a dose rate of 3.6 kGy/s.

droplet growth by condensation is always positive and inversely proportional to the droplet size and time due to diffusion-limited transport of vapor to the surface (eq 9). This leads to the observed decay in growth rate due to condensation over time. Conversely, the contribution of radiolysis-induced evaporation to the droplet growth rate is negative and directly proportional to the droplet radius. The production of hydrogen is a homogeneous process with a rate that is proportional to the irradiated droplet volume (eq 8); so as the droplet grows in volume over time, the hydrogen generation rate and the negative contribution to growth rate increase in magnitude. In other words, as the droplet size increases due to electric field-induced condensation, larger hydrogen production rates slow droplet growth and eventually lead to evaporation.

The critical point fitting procedure yielded an electric field magnitude of $|E| = (6.3 \pm 0.5) \times 10^8$ V/m. This value was consistent with the modified Kelvin equation (*cf.* Figure 4a), which showed that the vapor pressure of water was depressed significantly below the equilibrium value only for electric fields $>10^7$ V/m. We reiterate that the required silicon nitride conductivity to achieve this electric field in the electrostatic simulations was within the range of expected values. The best fit value for the combined diffusivity and contact angle parameter was $\varphi = 2 \times 10^{-13}$ m^2/s. Combining the macroscopic contact angle of water on silicon nitride of $\theta = 51°$ and the commonly accepted value of water vapor diffusivity of $D_v^* \sim 10^{-5}$ m^2/s yields the theoretical values of $g(\theta) = 0.13$ and $\varphi \approx 10^{-6}\frac{\mathrm{m}^2}{\mathrm{s}}$. As $g(\theta)$ is restricted to values of 0.1−1, the water vapor diffusivity obtained by the model fit was 7 orders of magnitude lower than the expected value. Prior work has indicated that diffusion coefficients tend to be smaller during liquid-phase TEM experiments, in some cases >5 orders of magnitude smaller compared to expected values.[33−35] A potential explanation for the decreased water vapor diffusion coefficient is the formation of positively charged water vapor molecules *via* inelastic electron scattering in the vapor ($H_2O(v) \rightarrow^{e^-} H_2O^+(v) + e^-$). Prior work has shown that >60% of water vapor molecules can be converted to positive ions upon electron irradiation.[36] Positively charged water ions will be repelled from the positively charged silicon nitride surface, which will effectively decrease the diffusion coefficient and the water vapor flux to the droplet surface. The electric field generates a significant Coulombic force on positively charged water vapor molecules, $F_{\mathrm{Coulombic}} = e|E|_y = 1 \times 10^{-10}$ N, which is about an order of magnitude larger than the kinetic energy, supporting the idea that charge repulsion leads to a decrease in the effective diffusion coefficient of water vapor.

Fitting of the model to the droplet growth kinetics yielded a hydrogen production rate of $R_{H_2} = 0.24$ mM/s. Kinetic simulations considering homogeneous radiolysis of the water droplet by primary 200 keV electrons predicted the steady-state hydrogen gas concentration in the droplet to be 0.09 mM, which is about 10% of the solubility limit in water (see Experimental Methods and Supporting Information, Section 6, for simulation details). This result suggests that the 200 keV TEM beam electrons did not cause overall conversion of liquid water to hydrogen gas (Figure 6a). However, it is likely that the commonly accepted *G*-values used for the radiolysis kinetic model (Table S1), which are empirical parameters measured at a low dose rate, were not accurate for the high electron dose rate of the TEM beam.[17] Prior work has shown that the high dose rates used during TEM lead to spur overlap during initial stages of radiolysis,[17,26] which increases the *G*-value for hydrogen production. Likewise, this initial calculation ignored impacts of the silicon nitride membranes enclosing the liquid cell, which produce low-energy secondary and backscattered electrons (SBE) that enhance radiolytic yields in water.[37] Simulations of SBE-induced radiolysis of water estimated that the hydrogen gas concentration increased monotonically above the saturation level after a few seconds of irradiation (Figure 6b) and that the average hydrogen generation rate was about 0.3 mM/s over the time period of droplet evaporation (Figure 6c). Despite the beam current of SBEs being 2 orders of magnitude lower than the 200 keV TEM beam electrons, the increased stopping power and hydrogen *G*-value led to significantly enhanced hydrogen yield compared to 200 keV electrons. Importantly, these calculations suggest that the silicon nitride membranes are significant sources of SBEs that, despite relatively low beam current due to their low yield, can have an outsized effect on hydrogen gas production in water during VPTEM. Finally, fitting produced an average temperature of 310 ± 0.4 K during droplet growth. Due to the nature of the fitting, it is not known whether the temperature increase was due to beam heating or the latent heat of water condensation. However, the constant temperature during droplet growth suggests that electron beam heating was not a significant factor in the growth and evaporation of water droplets.

CONCLUSIONS

In conclusion, we have visualized nanoscale water droplet nucleation, growth, and evaporation in electric fields with VPTEM. Droplet growth was consistent with electric field-induced water vapor pressure depression due to electron beam charging of the silicon nitride window surfaces, while evaporation was consistent with radiolytic conversion of water to hydrogen gas. Droplet temperatures did not

https://doi.org/10.1021/acs.jpca.2c08187
J. Phys. Chem. A 2023, 127, 2545−2553

significantly deviate from room temperature, which suggests that beam-induced heating did not have a significant impact on droplet growth or evaporation. There are several expected impacts of this work. First, it demonstrates a TEM method to image the dynamics of nanoscale vapor−liquid equilibrium phenomena under strong electric fields, which is important to understand the behavior of water in thunderstorms and clouds and the physics of electric field capture of atmospheric moisture. Second, this work developed models that provided experimental and theoretical estimates of radiolytic conversion of water to hydrogen and electron beam-induced electric fields. Taken together, the consistency of the electrostatic simulation, mass balance model, and radiolysis kinetics model provided strong evidence for the proposed mechanism. In terms of atmospheric processes, this work showed that subsaturated water can condense during VPTEM due to electric field-induced supersaturation. This method could prove useful for investigating water condensation on water insoluble and low hygroscopicity aerosol particles that only condense water under supersaturated conditions.[38] Water droplet growth kinetics observed by VPTEM were drastically slower than expected under conventional atmospheric conditions due to decreased water vapor diffusion rates and radiolytic hydrogen production. Taken together, these results are expected to provide a baseline understanding that will enable delineating electron beam−sample interactions from the aerosol phenomena of interest and correcting for electron beam effects on physical parameters like temperature and humidity in more complex aerosol-phase systems, such as water condensation on atmospheric aerosols.

■ ASSOCIATED CONTENT

Supporting Information

The Supporting Information is available free of charge at https://pubs.acs.org/doi/10.1021/acs.jpca.2c08187.

VPTEM sample preparation; TEM current measurement; data acquisition and analysis; droplet and nucleation growth model derivation; temperature curves from calculated fitting parameters; and details of recorded VPTEM movies (PDF)

Water influx and bubble formation in the sample cell (AVI)

Electron beam-induced water droplet nucleation and evaporation (uncropped TEM data) (AVI)

Replicate of electron beam-induced water droplet nucleation and evaporation (AVI)

■ AUTHOR INFORMATION

Corresponding Authors

Akua Asa-Awuku − *Department of Chemical and Biomolecular Engineering, University of Maryland, College Park, College Park, Maryland 20742, United States;* orcid.org/0000-0002-0354-8368; Email: asaawuku@umd.edu

Taylor J. Woehl − *Department of Chemical and Biomolecular Engineering, University of Maryland, College Park, College Park, Maryland 20742, United States;* orcid.org/0000-0002-4000-8280; Email: tjwoehl@umd.edu

Authors

Yuhang Wang − *Department of Chemistry and Biochemistry, University of Maryland, College Park, College Park, Maryland 20742, United States*

Dewansh Rastogi − *Department of Chemical and Biomolecular Engineering, University of Maryland, College Park, College Park, Maryland 20742, United States;* orcid.org/0000-0002-5416-0048

Kotiba Malek − *Department of Chemical and Biomolecular Engineering, University of Maryland, College Park, College Park, Maryland 20742, United States*

Jiayue Sun − *Department of Chemistry and Biochemistry, University of Maryland, College Park, College Park, Maryland 20742, United States*

Complete contact information is available at: https://pubs.acs.org/10.1021/acs.jpca.2c08187

Author Contributions

Y.W. and D.R. contributed equally. T.J.W. and A.A.-A. conceived of the study and supervised all aspects. J.S. performed the VPTEM imaging experiments. Y.W., K.M., J.S., and D.R. prepared the samples. T.J.W. and Y.W. analyzed the TEM data. All authors provided input on data interpretation. T.J.W., Y.W., D.R., and A.A.-A. developed the theoretical models. Y.W., D.R., and T.J.W. prepared the figures and wrote the manuscript. All authors contributed to revision of the manuscript.

Notes

The authors declare no competing financial interest.

■ ACKNOWLEDGMENTS

This work was supported by the National Science Foundation under grant no. 2003927. The authors thank Kyle Sendgikoski for assistance in measuring the electron beam current and John Cumings for useful discussions on electron beam charging. The authors acknowledge the staff at the University of Maryland AIM Lab for their assistance with electron microscopy imaging.

■ REFERENCES

(1) Gabyshev, D. N.; Fedorets, A. A.; Aktaev, N. E.; Klemm, O.; Andreev, S. N. Acceleration of the Condensational Growth of Water Droplets in an External Electric Field. *J. Aerosol Sci.* **2019**, *135*, 103−112.

(2) Gabyshev, D. N.; Fedorets, A. A.; Klemm, O. Condensational Growth of Water Droplets in an External Electric Field at Different Temperatures. *Aerosol Sci. Technol.* **2020**, *54*, 1556−1566.

(3) Wang, P.; Li, C.; Zhang, M.; Li, J.; Liu, Z.; Yang, Y.; Yu, K.; Pan, Y. Synergistic Effect of Charges and Electric Field: Water Droplet Condensation and Coalescence in a Sub-saturated Cloud Chamber. *Plasma Sources Sci. Technol.* **2020**, *29*, 045005.

(4) Miljkovic, N.; Preston, D. J.; Enright, R.; Wang, E. N. Electric-Field-Enhanced Condensation on Superhydrophobic Nanostructured Surfaces. *ACS Nano* **2013**, *7*, 11043−11054.

(5) Damak, M.; Varanasi, K. K. Electrostatically Driven Fog Collection using Space Charge Injection. *Sci. Adv.* **2018**, *4*, No. eaao5323.

(6) Gómez-Moñivas, S.; Sáenz, J. J.; Calleja, M.; García, R. Field-Induced Formation of Nanometer-Sized Water Bridges. *Phys. Rev. Lett.* **2003**, *91*, 056101.

(7) Orejon, D.; Sefiane, K.; Shanahan, M. E. R. Evaporation of Nanofluid Droplets with Applied DC Potential. *J. Colloid Interface Sci.* **2013**, *407*, 29−38.

(8) Butt, H.-J.; Untch, M. B.; Golriz, A.; Pihan, S. A.; Berger, R. Electric-field-induced Condensation: An Extension of the Kelvin

Equation. *Phys. Rev. E: Stat., Nonlinear, Soft Matter Phys.* **2011**, *83*, 061604.
(9) Vancauwenberghe, V.; Di Marco, P.; Brutin, D. Wetting and Evaporation of a Sessile Drop under an External Electrical Field: A Review. *Colloids Surf., A* **2013**, *432*, 50−56.
(10) Vas, J. V.; Cadete Santos Aires, F. J.; Ehret, E.; Landrivon, E.; Duchamp, M.; Epicier, T. Water Condensation / Evaporation Experiments in ETEM using a Thermoelectric Microcooler. *Microsc. Microanal.* **2022**, *28*, 818−819.
(11) Sacha, G. M.; Verdaguer, A.; Salmeron, M. Induced Water Condensation and Bridge Formation by Electric Fields in Atomic Force Microscopy. *J. Phys. Chem. B* **2006**, *110*, 14870−14873.
(12) Levin, B. D. A.; Haiber, D.; Liu, Q.; Crozier, P. A. An Open-Cell Environmental Transmission Electron Microscopy Technique for In Situ Characterization of Samples in Aqueous Liquid Solutions. *Microsc. Microanal.* **2020**, *26*, 134−138.
(13) Ross, F. M. Opportunities and Challenges in Liquid Cell Electron Microscopy. *Science* **2015**, *350*, aaa9886.
(14) Mirsaidov, U. M.; Zheng, H.; Bhattacharya, D.; Casana, Y.; Matsudaira, P. Direct Observation of Stick-slip Movements of Water Nanodroplets Induced by an Electron Beam. *Proc. Natl. Acad. Sci. U.S.A.* **2012**, *109*, 7187−7190.
(15) Anand, U.; Ghosh, T.; Aabdin, Z.; Koneti, S.; Xu, X.; Holsteyns, F.; Mirsaidov, U. Dynamics of Thin Precursor Film in Wetting of Nanopatterned Surfaces. *Proc. Natl. Acad. Sci. U.S.A.* **2021**, *118*, No. e2108074118.
(16) Yang, J.; Alam, S. B.; Yu, L.; Chan, E.; Zheng, H. Dynamic Behavior of Nanoscale Liquids in Graphene Liquid Cells Revealed by In Situ Transmission Electron Microscopy. *Micron* **2019**, *116*, 22−29.
(17) Grogan, J. M.; Schneider, N. M.; Ross, F. M.; Bau, H. H. Bubble and Pattern Formation in Liquid Induced by an Electron Beam. *Nano Lett.* **2014**, *14*, 359−364.
(18) Shin, D.; Park, J. B.; Kim, Y.-J.; Kim, S. J.; Kang, J. H.; Lee, B.; Cho, S.-P.; Hong, B. H.; Novoselov, K. S. Growth Dynamics and Gas Transport Mechanism of Nanobubbles in Graphene Liquid Cells. *Nat. Commun.* **2015**, *6*, 6068.
(19) Bae, Y.; Kang, S.; Kim, B. H.; Lim, K.; Jeon, S.; Shim, S.; Lee, W. C.; Park, J. Nanobubble Dynamics in Aqueous Surfactant Solutions Studied by Liquid-Phase Transmission Electron Microscopy. *Engineering* **2021**, *7*, 630−635.
(20) Woehl, T. J.; Jungjohann, K. L.; Evans, J. E.; Arslan, I.; Ristenpart, W. D.; Browning, N. D. Experimental Procedures to Mitigate Electron Beam Induced Artifacts during in situ Fluid Imaging of Nanomaterials. *Ultramicroscopy* **2013**, *127*, 53−63.
(21) Schneider, N. M.; Norton, M. M.; Mendel, B. J.; Grogan, J. M.; Ross, F. M.; Bau, H. H. Electron−Water Interactions and Implications for Liquid Cell Electron Microscopy. *J. Phys. Chem. C* **2014**, *118*, 22373−22382.
(22) Fritsch, B.; Hutzler, A.; Wu, M.; Khadivianazar, S.; Vogl, L.; Jank, M. P. M.; März, M.; Spiecker, E. Accessing Local Electron-beam Induced Temperature Changes during In Situ Liquid-phase Transmission Electron Microscopy. *Nanoscale Adv.* **2021**, *3*, 2466−2474.
(23) Fritsch, B.; Zech, T. S.; Bruns, M. P.; Körner, A.; Khadivianazar, S.; Wu, M.; Zargar Talebi, N.; Virtanen, S.; Unruh, T.; Jank, M. P. M.; et al. Radiolysis-Driven Evolution of Gold Nanostructures − Model Verification by Scale Bridging In Situ Liquid-Phase Transmission Electron Microscopy and X-Ray Diffraction. *Adv. Sci.* **2022**, *9*, 2202803.
(24) Woehl, T. J.; Moser, T.; Evans, J. E.; Ross, F. M. Electron-beam-driven Chemical Processes during Liquid Phase Transmission Electron Microscopy. *MRS Bull.* **2020**, *45*, 746−753.
(25) Woehl, T. J.; Abellan, P. Defining the Radiation Chemistry during Liquid Cell Electron Microscopy to Enable Visualization of Nanomaterial Growth and Degradation Dynamics. *J. Microsc.* **2017**, *265*, 135−147.
(26) Wang, M.; Park, C.; Woehl, T. J. Quantifying the Nucleation and Growth Kinetics of Electron Beam Nanochemistry with Liquid Cell Scanning Transmission Electron Microscopy. *Chem. Mater.* **2018**, *30*, 7727−7736.
(27) Pastina, B.; LaVerne, J. A. Effect of Molecular Hydrogen on Hydrogen Peroxide in Water Radiolysis. *J. Phys. Chem. A* **2001**, *105*, 9316−9322.
(28) Cazaux, J. Correlations between Ionization Radiation Damage and Charging Effects in Transmission Electron Microscopy. *Ultramicroscopy* **1995**, *60*, 411−425.
(29) Jiang, N. Note on In Situ (Scanning) Transmission Electron Microscopy Study of Liquid Samples. *Ultramicroscopy* **2017**, *179*, 81−83.
(30) Škoro, N.; Marić, D.; Malović, G.; Graham, W. G.; Petrović, Z. L. Electrical Breakdown in Water Vapor. *Phys. Rev. E: Stat., Nonlinear, Soft Matter Phys.* **2011**, *84*, 055401.
(31) Kim, S.; Kim, D.; Kim, J.; An, S.; Jhe, W. Direct Evidence for Curvature-Dependent Surface Tension in Capillary Condensation: Kelvin Equation at Molecular Scale. *Phys. Rev. X* **2018**, *8*, 041046.
(32) Viisanen, Y.; Strey, R.; Reiss, H. Homogeneous Nucleation Rates for Water. *J. Chem. Phys.* **1993**, *99*, 4680−4692.
(33) Woehl, T. J.; Prozorov, T. The Mechanisms for Nanoparticle Surface Diffusion and Chain Self-Assembly Determined from Real-Time Nanoscale Kinetics in Liquid. *J. Phys. Chem. C* **2015**, *119*, 21261−21269.
(34) Yesibolati, M. N.; Mortensen, K. I.; Sun, H.; Brostrøm, A.; Tidemand-Lichtenberg, S.; Mølhave, K. Unhindered Brownian Motion of Individual Nanoparticles in Liquid-Phase Scanning Transmission Electron Microscopy. *Nano Lett.* **2020**, *20*, 7108−7115.
(35) White, E. R.; Singer, S. B.; Augustyn, V.; Hubbard, W. A.; Mecklenburg, M.; Dunn, B.; Regan, B. C. In Situ Transmission Electron Microscopy of Lead Dendrites and Lead Ions in Aqueous Solution. *ACS Nano* **2012**, *6*, 6308−6317.
(36) Melton, C. E. Radiolysis of Water Vapor in a Wide Range Radiolysis Source of a Mass Spectrometer. I. Individual and Total Cross Sections for the Production of Positive Ions, Negative Ions, and Free Radicals by Electrons. *J. Phys. Chem.* **1970**, *74*, 582−587.
(37) Gupta, T.; Schneider, N. M.; Park, J. H.; Steingart, D.; Ross, F. M. Spatially Dependent Dose Rate in Liquid Cell Transmission Electron Microscopy. *Nanoscale* **2018**, *10*, 7702−7710.
(38) Mao, C. N.; Gohil, K.; Asa-Awuku, A. A. A Single-parameter Hygroscopicity Model for Functionalized Insoluble Aerosol Surfaces. *Atmos. Chem. Phys.* **2022**, *22*, 13219−13228.

https://doi.org/10.1021/acs.jpca.2c08187
J. Phys. Chem. A 2023, 127, 2545−2553